Published in "Journal of Electron Spectroscopy and Related Phenomena 233(): 11–21, 2019"
which should be cited to refer to this work.

Cross section ratios of double-to-single *K*-shell ionization induced by electron impact in metallic Sc, Cr and Cu targets

F. Zeeshan, J.-Cl. Dousse*, J. Hoszowska

Department of Physics, University of Fribourg, CH-1700 Fribourg, Switzerland

ARTICLE INFO

Keywords:
Electron impact induced atomic ionization
X-ray hypersatellites
Double-to-single *K*-shell ionization cross section ratios
High energy resolution X-ray spectroscopy

ABSTRACT

The double *K*-shell ionization of Sc, Cr and Cu induced by electron impact was investigated via high energy resolution measurements of the $K\alpha$ diagram transitions and the transitions resulting from the radiative decay of *K*-shell double vacancy states, namely the $K^h\alpha$ hypersatellites. For Sc, the $K\beta$ diagram lines and $K^h\beta$ hypersatellites were also measured. The measurements were carried out in-house with a von Hamos curved crystal spectrometer operated in the so-called direct geometry in which the anodes of Sc, Cr and Cu X-ray tubes were used as targets. For each element, the electron kinetic energy was chosen to be about twice the threshold energy for the double *1s* ionization. The double-to-single ionization cross-sections ratios P_{KK} were deduced from the hypersatellite-to-diagram line yield ratios, corrected beforehand for the self-absorption of the X-rays in the target and the energy dependent efficiency of the spectrometer. The obtained ratios are discussed and compared to other P_{KK} values found in the literature for electrons and photons.

1. Introduction

The double *K*-shell ionization of neutral elements leads to the production of so-called hollow *K*-shell atoms, i.e., atoms with an empty *K*-shell while the other outer shells are occupied. The double *K*-shell ionization can be produced by collisions with energetic heavy ions (see, e.g., [1]), light charged particles such as α particles (see, e.g., [2]), protons (see, e.g., [3]) and electrons (see, e.g., [4]) or by impact with photons (see, e.g., [5]). In the latter case, the advent of third generation synchrotron radiation (SR) sources and the more recent development of X-ray free electron laser (XFEL) facilities have given a new boost to the domain.

As in the photoelectric effect a single photon interacts with a single atomic electron and because the photon disappears after the interaction, the removal of the second electron requires another process. Actually two different mechanisms contribute to the second ionization, namely the shake [6] and the knock-out (KO) [7] processes. In the shake process, the second electron is removed due to the abrupt change of the atomic potential following the ionization of the first electron. The shaken electron can be ejected into the continuum or promoted into an unfilled outer shell. In the first case, the effect is named shake-off (SO), in the second one shake-up (SU). The KO mechanism is a two step process in which the first ionized electron hits a second bound electron which is then ejected from the atom. This electron–electron inelastic scattering process is also named Two-Step-One (TS1) process. The TS1 process is the dominant effect at low photon energies, whereas the shake mechanism prevails at high photon energies [8,5]. In the XFEL case, the extremely short (10^{-15} s), micro-focused and very intense X-ray pulses allow to produce double *K*-shell vacancy states by the absorption of two photons by the same atom [9–13].

The double *K*-shell ionization induced by impact with electrons can be also explained by the SO/SU and TS1 processes. Another mechanism, the Two-Step-Two (TS2) process, may contribute to the production of double vacancy states. In the TS2 process, the two bound electrons are ionized by the incoming electron via two consecutive inelastic scattering processes. The SO/SU, TS1 and TS2 processes are energetically allowed only if the energy needed to ionize the second bound electron is provided by the incoming electron. In other words, the electron-induced double *K*-shell ionization requires that the kinetic energy of the incoming electron is bigger or equal to the threshold energy for the double *1s* ionization.

As commercial electron guns cannot be operated usually above 20 kV, most available electron-induced double *K*-shell ionization data concern low-Z elements [4,14]. An alternative method for studying the double *K*-shell ionization induced by electron impact consists to replace the electron guns by X-ray tubes that can be operated currently up to 60 kV or higher and use the anodes of the latter as sources of radiation. This permits to extend *K*-hypersatellite measurements induced by

* Corresponding author at: Department of Physics, University of Fribourg, Chemin du Musée 3, CH-1700 Fribourg, Switzerland
E-mail address: jean-claude.dousse@unifr.ch (J.-C. Dousse).

electron impact to heavier elements [15,16].

The radiative decay of hollow K-shell atoms leads to the emission of so-called $K^h\alpha$ and $K^h\beta$ hypersatellite X-ray lines which are shifted towards higher energies as compared to the parent $K\alpha$ and $K\beta$ diagram transitions decaying atoms with a single $1s$ vacancy. It is well known that the $I(K\alpha_1)/I(K\alpha_2)$ intensity ratio is about 2 for all elements throughout the periodic table. This is no more true for hypersatellite transitions because the $K^h\alpha_1$ hypersatellite which corresponds to the $1^1S_0 \rightarrow 2^3P_1$ spin-flip transition ($\Delta S = 1$) is forbidden by the $E1$ selection rules in the pure LS coupling. The $K^h\alpha_1$ transition is, however, allowed in the jj coupling. On the other hand, the $K^h\alpha_2$ hypersatellite which corresponds to the $1^1S_0 \rightarrow 2^1P_1$ transition ($\Delta S = 0$, i.e., no spin flip) is allowed by the $E1$ selection rules in both coupling schemes. Thus, for hypersatellites the $I(K^h\alpha_1)/I(K^h\alpha_2)$ intensity ratio is nearly zero for light elements, for which the LS coupling scheme prevails, while tending to the value of 2 for heavy elements for which the relevant coupling is the jj one. In the case of mid-heavy elements for which the intermediate coupling scheme applies, the $I(K^h\alpha_1)/I(K^h\alpha_2)$ intensity ratio grows progressively between these two extremes as a function of the atomic number Z. The same holds for the $I(K^h\beta_1)/I(K^h\beta_3)$ yield ratio since the $K^h\beta_1$ hypersatellite (spin-flip transition $1^1S_0 \rightarrow 3^3P_1$) is forbidden by the $E1$ selection rules in the LS coupling scheme and thus not observable for light elements, whereas the transition $1^1S_0 \rightarrow 3^1P_1$ corresponding to the $K^h\beta_3$ hypersatellite is allowed in both the LS and jj coupling schemes.

The double-to-single K-shell ionization cross section ratios P_{KK} can be derived from the hypersatellite-to-diagram line yield ratios. In the case of double photoionization the P_{KK} ratios were investigated extensively [5], many results from SR-based measurements being available in the literature. For electron-induced double K-shell ionization, however, P_{KK} values are more scarce and only available for three light elements (Na [17], Mg [14] and Al [4,18]) and two $3d$ elements (Cr and Fe [19]).

In this work, the $K\alpha$ hypersatellite X-ray spectra of Sc (Z = 21), Cr (Z = 24) and Cu (Z = 29) induced by electron impact were measured by means of high energy resolution spectroscopy. For Sc the extremely weak $K^h\beta$ hypersatellite could also be measured. Although Cr was already measured [19], the measurement was repeated in order to compare our results with previous ones for at least one element. For each element the electron kinetic energy was chosen to be around 2 times bigger than the threshold energy for the double $1s$ ionization. At this electron energy the double $1s$ ionization is indeed close to its maximum value. The double-to-single-ionization cross section ratios P_{KK} were derived from the measured relative intensities of the hypersatellites corrected beforehand for the self-absorption of the X-rays in the X-ray tube anodes and the energy dependent efficiency of the spectrometer.

2. Experiment

2.1. Von Hamos spectrometer

The measurements were performed by means of high energy resolution X-ray spectroscopy using the von Hamos bent crystal spectrometer of Fribourg [20]. In this spectrometer, a narrow slit placed in front of the sample represents the effective source of radiation (see Fig. 1). For the Sc measurements the spectrometer was equipped with a LiF(200) crystal, while a Si(220) crystal was employed for the Cr and Cu measurements. For the detection of the X-rays a back-illuminated CCD camera consisting of 1300 pixels in the direction of dispersion and 400 pixels in the vertical direction with a pixel resolution of 20 μm was employed. As the intensity of each CCD pixel is proportional to the deposited photon energy, good X-ray events were sorted by setting energy windows corresponding to the transitions of interest in the ADC spectrum of the CCD. This allowed us to minimize the background and suppress events corresponding to photons diffracted at higher orders. As the spatial resolution of 5 μm of the CCD was not really needed in this experiment, a binning of five juxtaposed pixels was performed to get spectra with higher intensities.

Present measurements were performed with the von Hamos spectrometer operated in the so-called direct setup. In this setup the sample is replaced by the anode of a side window X-ray tube. The X-ray tube is oriented so that the center of the electron beam spot on the anode, the center of the slit and the center of the crystal are all aligned along the direction determined by the central Bragg angle corresponding to the X-ray line to be measured (see Fig. 1). To reduce the scattering of the X-rays in the spectrometer chamber, a Cu collimator with a 20 mm high × 5 mm wide rectangular aperture was mounted on the nose of the X-ray tube in front of the Be window.

2.2. Intensity attenuation of the diagram lines

As the intensity of the radiation emitted by an X-ray tube is proportional to the electron current but not to the electric potential

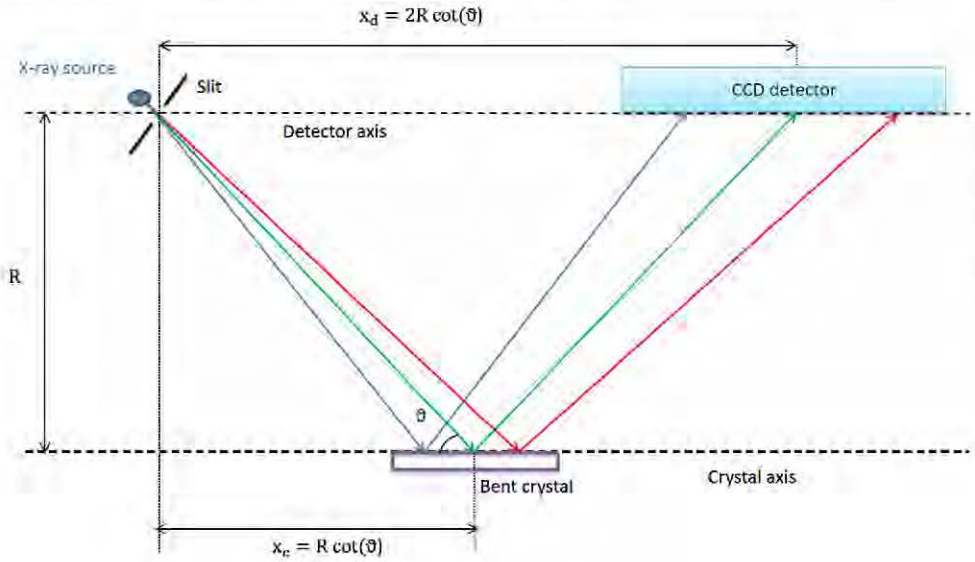

Fig. 1. Schematic drawing (top view) of the von Hamos spectrometer slit geometry. R stands for the radius of curvature of the crystal and ϑ for the central Bragg angle. The lengths x_c and x_d represent the distances, measured along the direction of dispersion, between the slit and the crystal and CCD, respectively. The X-ray source corresponds to the electron beam spot on the X-ray tube anode. (For interpretation of the references to color in this figure legend, the reader is referred to the web version of this article.)

difference between the cathode and the anode, the same high voltage had to be used for the measurements of the diagram and hypersatellite X-ray lines to get reliable intensity ratios. For the diagram lines, however, these high voltage values resulted in count rates that were too high for the CCD detector. The problem was solved by inserting absorbers (metallic foils) between the collimator and the Be window of the X-ray tube for the diagram line measurements. The metallic absorbers were chosen so that they did not produce X-ray fluorescence lines in the energy regions corresponding to the diagram transitions of the measured samples and their thicknesses were selected so that the count rate on the top of the $K\alpha_1$ or $K\beta_1$ line was kept below about 20 counts/s, a count rate for which the probability to observe multiple hits on the same CCD pixel is reasonably low (a few per mil).

The attenuation factors A of the employed absorbers were determined experimentally, using the following method. At first, the highest voltage U_0 and current i_0 of the X-ray tube for which the count rate measured without absorber on the top of the $K\alpha_1$ or $K\beta_1$ line was still smaller than 20 counts/s were determined. Then the attenuation factor of the absorber needed to keep the count rate of the $K\alpha_1$ or $K\beta_1$ line below the value of 20 counts/s at the high voltage U and current i used for the hypersatellite measurement was estimated and the absorber was chosen. The effective attenuation factor of the latter was then determined experimentally from the intensity ratio of the $K\alpha_{1,2}$ or $K\beta_{1,3}$ lines measured at U_0 and i_0 without and with absorber. For the $K\alpha_1$ lines of Sc and Cu, however, the needed attenuation factors were so big that the two lines measured with the corresponding absorbers at $U_0 \times i_0$ were too weak to be observed. To bypass this problem, the $K\alpha_{1,2}$ lines of Sc and Cu were also measured at intermediate voltages U_1 ($U_0 < U_1 < U$) with the main absorbers (intensities I_{abs}) and with thinner absorbers (intensities I_1) as well as at the voltages U_0 with the thinner absorbers (intensity I_2) and without absorber (intensities I_0). As I_0 could not be measured at the voltage U_1 (too high counting rate), the values $I_0(U_1)$ were obtained by multiplying the measured intensities $I_0(U_0)$ by the ratios I_1/I_2 normalized beforehand, when necessary, for the differences in the X-ray tube current, and the attenuation factors of the main absorbers in the Sc and Cu measurements were then determined using the following relation:

$$A = \frac{I_0 \frac{i_1}{I_2}}{I_{abs}}. \quad (1)$$

The absorbers used in the different measurements, the X-ray tube parameters $U_0 \times i_0$, $U_1 \times i_1$ and U × i as well as the corresponding attenuation factors A are presented in Table 1. The errors on the attenuation factors originate from the errors of the fitted intensities.

To crosscheck the accuracy of the obtained attenuation factors, the latter were also derived from the known thicknesses of the absorbers and the mass absorption coefficients quoted in the NIST XCOM database [21]. Relative deviations smaller than 5% were found for all absorbers.

3. Data analysis

3.1. Fitting procedure

The spectra were fitted by means of a nonlinear least squares fitting program using the software package PeakFit® (SYSTAT Software Inc., Richmond, USA). As the convolution of the Gauss function representing the instrumental response of the spectrometer with the Lorentz function describing the natural line shape of an X-ray transition results into a Voigt function [22], all diagram and hypersatellite lines were fitted with Voigtian profiles. In most cases, the energies, intensities and Lorentzian widths of the measured transitions as well as the background parameters were let free in the fitting procedure, whereas the instrumental broadening parameters were kept fixed at their known values.

As mentioned before the $K^h\alpha_1$ hypersatellites are very weak for light elements. For this reason, the $K^h\alpha_1$ intensities of Sc and Cr had to be kept fixed in the fits. The intensities were locked at the values obtained from the $I(K^h\alpha_1)/I(K^h\alpha_2)$ yield ratios calculated by Costa [23]. Furthermore, the same natural widths were assumed first for both hypersatellites using the option of parameters' sharing provided by the PeakFit® program. In the final fit, however, the Lorentzian width of the $K^h\alpha_1$ line was fixed at the value given by the first fit minus the difference between the widths of the L_2 and L_3 atomic levels.

3.1.1. $K^h\alpha$ and $K^h\beta$ spectra of Sc

The fitted $K\alpha$ hypersatellite spectrum of Sc is presented in Fig. 2a). The background was fitted with a linear function. The peak around 4296 eV corresponds to the $K^h\alpha_2$ hypersatellite and the weak bump around 4309 eV to the $K^h\alpha_1$. The latter is superimposed on the low energy tails of *KMM* radiative Auger transitions. Radiative Auger transitions are Auger transitions which are characterized by the simultaneous emission of an Auger electron and a photon [24,6,25]. More specifically, in *KMM* radiative Auger transitions, a *M*-shell electron fills the *K*-shell vacancy and another *M*-shell electron and a photon are simultaneously emitted by the atom. As the energy of the transition is shared between the electron and the photon, *KMM* radiative Auger structures are continuous and appear on the low energy sides of the $K\beta$ diagram lines. Since Auger transition probabilities are bigger for light elements, the radiative Auger effect (RAE) is more important for low-*Z* elements like Sc. As shown in Fig. 2a), the $K^h\alpha_2$ hypersatellite is well separated from the *KMM* RAE transitions but not the $K^h\alpha_1$.

The Sc $K^h\alpha_2$ hypersatellite line was fitted with one Voigtian whose energy, intensity and Lorentzian width could be let free in the fit. The $K^h\alpha_1$ hypersatellite was also fitted with one Voigtian but only the energy could be used as free fitting parameter. Regarding the *KMM* radiative Auger structure, the latter was fitted with two Voigtians whose energies, intensities, Lorentzian and Gaussian widths were let free in the fit.

The $K^h\beta$ hypersatellite spectrum of Sc measured at 20 kV could not be fitted in a straightforward way because the net count rate on the top

Table 1
Attenuation factors A of the absorbers employed to diminish the intensities of the diagram lines. The X-ray tube voltages and currents used in these measurements are also given. For the $K\alpha$ measurements of Sc and Cu the intensities I_1 and I_2 (see text) were obtained using 10.6 mg/cm^2 Al and 13.7 mg/cm^2 Au absorbers, respectively.

Measurement	$U_0 \times i_0$ [kV × mA]	$U_1 \times i_1$ [kV × mA]	$U \times i$ [kV × mA]	Absorber (thickness) [mg/cm^2]	A
Sc $K\alpha$	4.5 × 1	6.0 × 2	20.0 × 10	Al (16.3) + Ta (3.3)	4800 ± 38
Sc $K\beta$	6.5 × 1	–	20.0 × 10	Al (18.9)	144 ± 4
Cr $K\alpha$	6.0 × 1	–	26.5 × 10	Au (13.7)	2462 ± 28
			60.0 × 10	Au (13.7)	2462 ± 28
Cu $K\alpha$	9.0 × 1	32.0 × 1	39.6 × 10	Au (38.0)	2528 ± 20

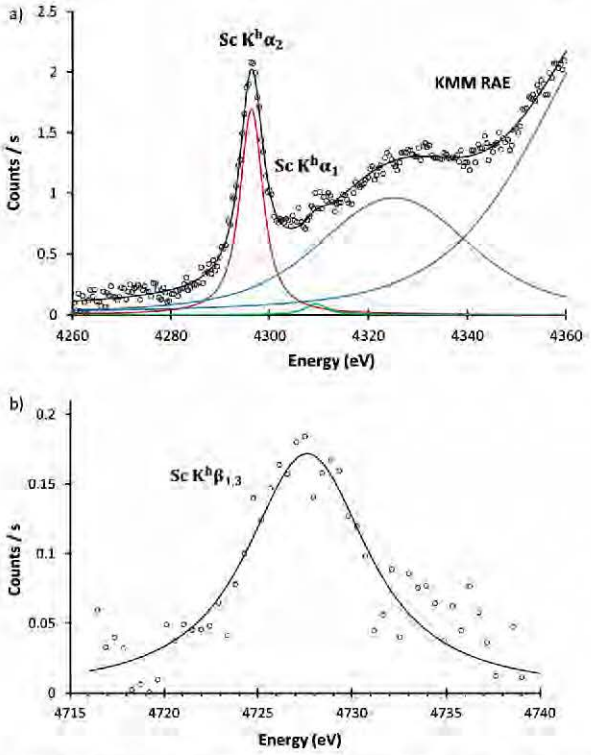

Fig. 2. (a) $K\alpha$ hypersatellite spectrum of Sc measured at 20 kV × 10 mA with a LiF(200) crystal. The measured spectrum is represented by the open circles and the total fit by the black solid line. The red and green curves stand for the fits of the $K^h\alpha_2$ and $K^h\alpha_1$ hypersatellites, respectively, and the blue solid lines for the two Voigtians used to fit the *KMM* RAE structures. To better show the weak hypersatellite transitions, the background determined by the fit was subtracted from the experimental data and the fitted components. (b) $K\beta$ hypersatellite spectrum of Sc measured using the same crystal and X-ray tube high voltage. The measured spectrum (after subtraction of the background according to the procedure described in the text) is represented by the open circles and the total fit by the black solid line. (For interpretation of the references to color in this figure legend, the reader is referred to the web version of this article.)

of the hypersatellite line was only about 0.2 count/s, i.e., 150 times smaller than the average count rate of the background (30 counts/s). In addition some fake structures were observed in the background as a result of intensity inhomogeneities of the electron beam spot on the X-ray tube anode. As in the von Hamos slit geometry different parts of the crystal surface see different parts of the electron beam spot on the anode, the shape of the spectrum can be indeed affected by such inhomogeneities. To circumvent this problem, the spectrum was re-measured with the same setup except the high voltage of the X-ray tube which was set to 8 kV. The fake structures observed in the background of the 20 kV spectrum were also seen in the second spectrum but not the hypersatellite line since the maximum energy of the photons emitted by the tube at 8 kV was smaller than the double 1*s* ionization threshold energy. The intensity of the 8 kV spectrum was then multiplied by a scaling factor in order to get the best match with the 20 kV spectrum in the energy regions lying below and above the hypersatellite. Note that the contribution of the hypersatellite tails to the background in the overlapping regions used to determine the scaling factor was negligibly small due to the much weaker intensity of the hypersatellite as compared to the background. Finally, the re-scaled 8 kV spectrum was subtracted from the raw spectrum and the residual spectrum was fitted (see Fig. 2b). As shown, due to the subtraction of the two spectra, the data are very noisy. The $K^h\beta_{1,3}$ hypersatellite was fitted with a single Voigtian because the energy separation between the $K^h\beta_1$ and $K^h\beta_3$ components (1.4 eV according to [26]) is much smaller than the natural widths of the two components and because the intensity ratio between the forbidden $K^h\beta_1$ and allowed $K^h\beta_3$ hypersatellite transitions is only 0.047 [26]. Despite the poor statistics of the spectrum, the energy, intensity and Lorentzian width of the Voigtian could be used as free fitting parameters but the corresponding fit errors are rather large.

3.1.2. $K^h\alpha$ spectra of Cr

The $K\alpha$ hypersatellite spectrum of Cr was measured with a Si(220) crystal. The X-ray tube was operated first at 26.5 kV × 10 mA and then at 60.0 kV × 10 mA. To check the reliability of the experimental setup the spectrum collected at 60 kV was re-measured with another perfect crystal, namely Ge(220), and a HAPG(004) (Highly Annealed Pyrolytic Graphite) mosaic crystal.

The fit of the $K^h\alpha$ hypersatellite spectrum measured at 26.5 kV is depicted in Fig. 3a). The background was fitted with a linear function. The Voigtians at about 5650 eV and 5667 eV correspond to the $K^h\alpha_2$ and $K^h\alpha_1$ hypersatellites, respectively. As the $K^h\alpha_2$ line was found to evince some asymmetry on its low energy flank, this transition was fitted with two Voigtians. The energies, intensities and Lorentzian widths of the two Voigtians were let free in the fit. The $K^h\alpha_1$ line was fitted with one Voigtian with the energy as single free fitting parameter.

As the asymmetry of the $K^h\alpha_2$ hypersatellite was found to be broader and less intense in the spectrum collected with the same crystal at 60 kV, narrower and smaller for the measurement performed with the Ge(220) crystal and was not observed with the HAPG(004) crystal, the asymmetry was assumed to be due to background fluctuations originating from inhomogeinities in the intensity of the electron beam spot on the X-ray tube anode. The intensity of the Voigtian used to account for the asymmetry was therefore not taken into consideration in the determination of the hypersatellite intensity. Some excess of intensity was also found on the right hand side of the spectrum. This intensity excess is due to *KMM* RAE transitions. Note that the RAE intensity observed in the $K^h\alpha$ hypersatellite spectrum of Cr is much weaker than in the case of Sc as a consequence of the bigger atomic number of Cr and mostly because the energy difference between the upper edge of the KM_1M_1 RAE transition, the RAE transition with the lowest energy, and the $K^h\alpha_1$ hypersatellite is about 165 eV for Cr and only 66 eV for Sc [27].

The Cr $K\alpha$ hypersatellite measured with the Si(220) crystal at 60 kV × 10 mA is shown in Fig. 3b). The spectrum was fitted as the one measured at 26.5 kV. The spectra measured with the Ge(220) and HAPG(004) crystals are presented in Fig. 3c) and d), respectively. Similar fits as the one done for the spectrum measured with the Si(220) crystal were carried out except that no Voigtian was needed for the RAE structure, the latter being smeared out by the higher background observed in the measurements performed with these two crystals. In the spectrum measured with the Ge(220) crystal, an increase of the background at both ends of the $K^h\alpha$ hypersatellite region was observed. These intensity enhancements were accounted for by adding two Voigtians (black dotted lines) to the linear fit of the background. For the measurement with the HAPG crystal, the background was more regular so that it could be well fitted with a linear function. As no asymmetry nor RAE structures were observed in the spectrum, the latter could be well fitted using only two Voigtians, one for each hypersatellite.

3.1.3. $K^h\alpha$ spectra of Cu

The measured $K\alpha$ hypersatellite spectrum of Cu is represented in Fig. 4. The data were collected in second order of diffraction using a Si (220) crystal. The Cu anode X-ray tube was operated at 39.6 kV × 10 mA. As shown in Fig. 4, despite a longer acquisition time (125,000 s) than for Sc and Cr (30,000 s), the spectrum is rather noisy. The scatter of the experimental data originates from the statistical fluctuations of the background. The latter is mainly due to the high energy tails of the very strong $K\alpha_{1,2}$ diagram lines. Actually for the $K^h\alpha_2$ hypersatellite of Cu the peak-to-background ratio is only about 1:30 (see inset of Fig. 4), whereas the same ratio amounts to 1:6 for the Cr measurement performed at 60 kV.

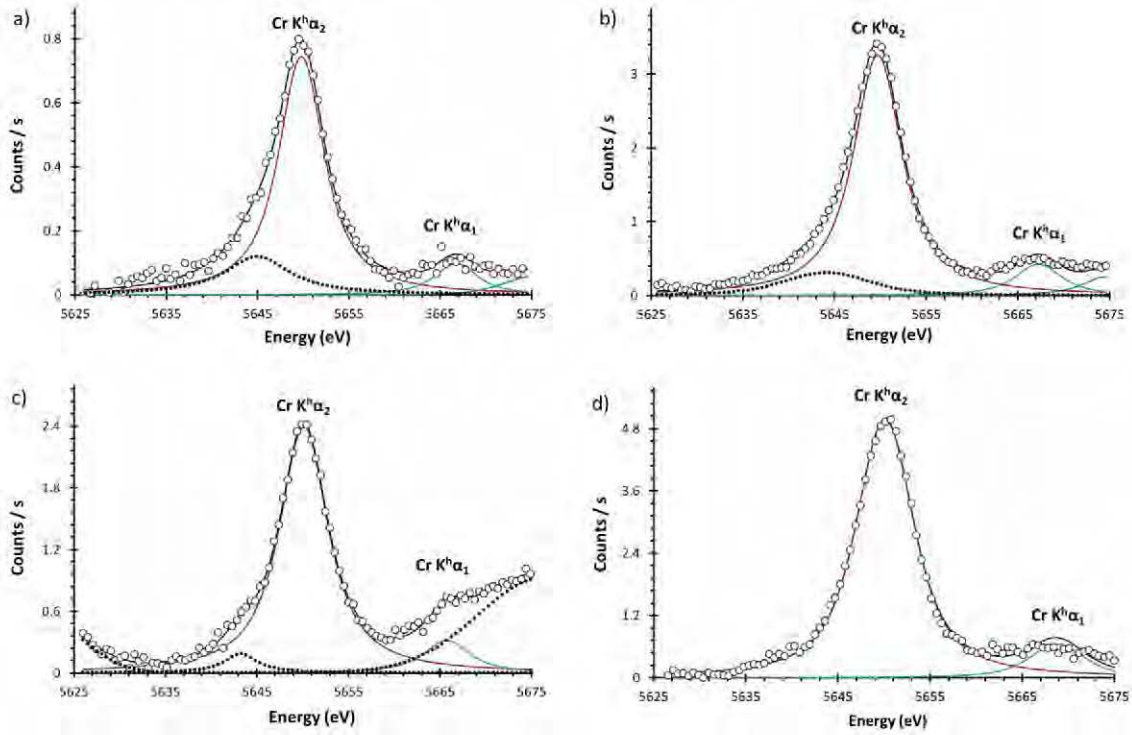

Fig. 3. (a) Cr *Kα* hypersatellite spectrum measured at 26.5 kV × 10 mA using a Si(220) crystal. The measured spectrum is represented by the open circles and the total fit by the black solid line. The red and green curves stand for the fits of the $K^h\alpha_2$ and $K^h\alpha_1$ hypersatellites, respectively. The black dotted line and the blue solid line (above 5667 eV) represent the Voigtians used to fit the $K^h\alpha_2$ asymmetry and the *KMM* RAE intensity, respectively. To better show the weak hypersatellite transitions, the background determined by the fit was subtracted from the experimental data and the fitted components. (b) Same as (a) but for the X-ray tube operated at 60 kV × 10 mA. (c) Same as (b) but measured with a Ge(220) crystal. The black dotted lines represent the tails of the Voigtians used in the fit to account for the intensity enhancements observed with this crystal at both ends of the hypersatellite spectrum. (d) Same as (b) but measured with a HAPG(004) crystal. (For interpretation of the references to color in this figure legend, the reader is referred to the web version of this article.)

The hypersatellites were fitted using one Voigtian for each transition. The parameters of both Voigtians could be let free in the fit except the Lorentzian width of the $K^h\alpha_1$ component which was fixed at the width of the $K^h\alpha_2$ hypersatellite minus the difference between the L_2 and L_3 atomic level widths (0.43 eV according to Ref. [28]). When both Lorentzian widths were let free in the fit, it was indeed found that the value of the $K^h\alpha_1$ width was about two times smaller than the one of the $K^h\alpha_2$ hypersatellite, which is physically not sound. In contrast to that, the intensity of the $K^h\alpha_1$ could be let free. The $K^h\alpha_1/K^h\alpha_2$ yield ratio deduced from the fit is (33.3 ± 4.6) %, a result well in line with the value of 32.5% predicted by the calculations of Costa et al. [23]. The best fit of the Cu hypersatellite spectrum was obtained when a third degree polynomial was employed for the background.

In order to check the accuracy of the fits, the energies and Lorentzian widths of the $K^h\alpha$ hypersatellites found in this work were compared to the corresponding values obtained with synchrotron

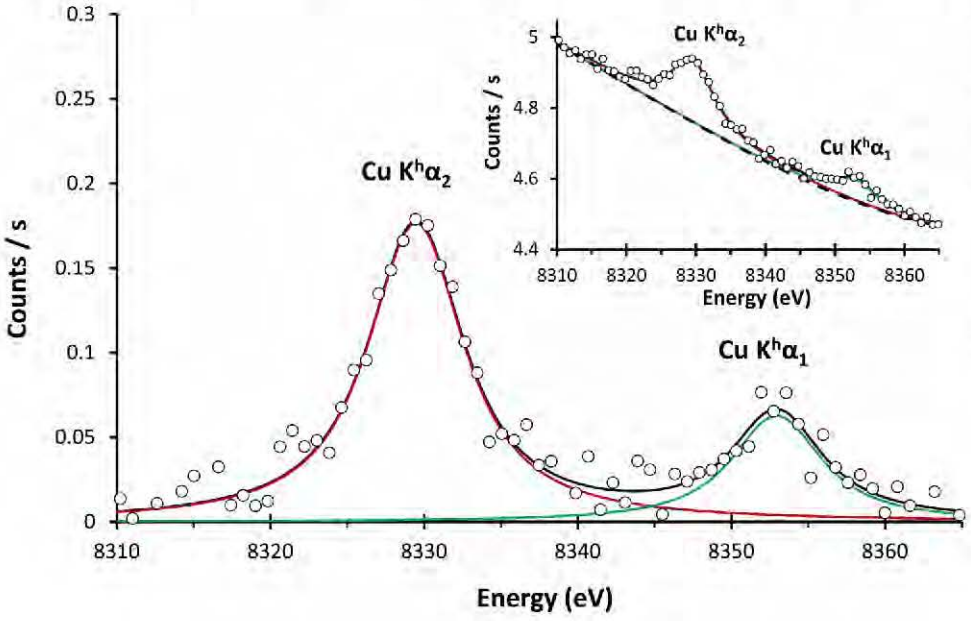

Fig. 4. Cu *Kα* hypersatellite spectrum measured at 39.6 kV × 10 mA using a Si(220) crystal in second order of diffraction. The measured spectrum is represented by the open circles and the total fit by the black solid line. The red and green curves stand for the fits of the $K^h\alpha_2$ and $K^h\alpha_1$ hypersatellites, respectively. To better show the weak hypersatellite transitions, the background determined by the fit was subtracted from the experimental data and the fitted components. The total spectrum including the background (dashed line) is depicted in the inset. (For interpretation of the references to color in this figure legend, the reader is referred to the web version of this article.)

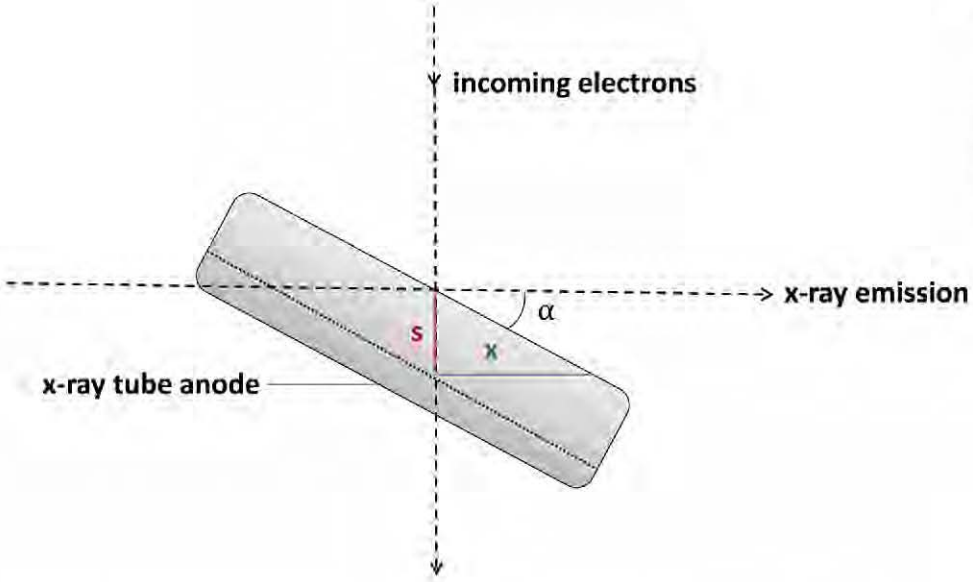

Fig. 5. Side view of the X-ray tube anode showing the vertical electron path, the penetration depth s and the distance $x = ctg(\alpha)s$ traveled by the X-rays to exit the anode. For the three X-ray tubes used in the present project the angle α was equal to 26°. (For interpretation of the references to color in this figure legend, the reader is referred to the web version of this article.)

radiation. An excellent agreement was found between our results and the ones reported for Sc by Hoszowska et al. [5] and for Cr and Cu by Diamant et al. [29]. For the $K^h\beta$ hypersatellite of Sc, for which no experimental data could be found in the literature, an energy of 4727.63(69) eV was obtained, i.e., an energy shift of 267.19(83) eV with respect to the parent diagram line, a result which is well in line with the theoretical prediction of 267.66 eV reported by Costa [26]. Regarding the Lorentzian width of the $K^h\beta$ hypersatellite of Sc, no experimental nor theoretical data is available in the literature for comparison. Nevertheless, the present value of (7.1 ± 1.1) eV looks quite reasonable since a width of 7.8 eV is reported in [30] for the $K^h\beta$ hypersatellite of Ti, the next higher Z element.

3.2. Intensity correction factors

3.2.1. Target self absorption

The correction factor accounting for the self absorption of the $K\alpha$ or $K\beta$ diagram X-rays in the anode of the X-ray tube can be written as follows:

$$\zeta_{K\alpha,K\beta} = \frac{\int_0^{h_K} \sigma_K(E_e(s)) e^{-\mu_{K\alpha,K\beta}\,\mathrm{ctg}(\alpha)s}\,\mathrm{ds}}{\int_0^{h_K} \sigma_K(E_e(s))\,\mathrm{ds}}, \tag{2}$$

where $E_e(s)$ represents the kinetic energy of the electron at the depth s of the anode, $\sigma_K(E_e)$ the energy dependent cross section of the electron-induced single K-shell ionization, α the angle made by the X-ray tube anode with respect to the horizontal plane (see Fig. 5) and h_K the depth at which $E_e(h_K) = E_K$, E_K being the threshold energy for a single K-shell ionization.

The correction factor for the self absorption of the $K^h\alpha$ or $K^h\beta$ hypersatellites is similarly given by:

$$\zeta_{K^h\alpha,K^h\beta} = \frac{\int_0^{h_{KK}} \sigma_{KK}(E_e(s)) e^{-\mu_{K^h\alpha,K^h\beta}\,\mathrm{ctg}(\alpha)s}\,\mathrm{ds}}{\int_0^{h_{KK}} \sigma_{KK}(E_e(s))\,\mathrm{ds}}, \tag{3}$$

with $\sigma_{KK}(E_e)$ standing for the cross section of the electron-induced double K-shell ionization and h_{KK} for the depth at which $E_e(h_{KK}) = E_{KK}$, E_{KK} corresponding to the threshold energy for a double K-shell ionization.

The energy loss of the electrons in the anode per length unit can be parametrized using the following equation:

$$\frac{\mathrm{dE}_e}{\mathrm{ds}} = -\kappa E_e^{-\nu}, \tag{4}$$

where κ and ν are two real positive constants. The latter were determined by a linear least squares fitting of the electron stopping powers calculated with the NIST ESTAR code [31] to the function:

$$\ln\left(\left|\frac{\mathrm{dE}_e}{\mathrm{ds}}\right|\right) = -\nu\,[\ln(E_e)] + \ln(\kappa). \tag{5}$$

The values ν and κ obtained from the fits are presented in Table 2. As the electron stopping powers calculated by the ESTAR code are given in MeVcm^2/g, the obtained penetration depths are expressed in g/cm^2. The kinetic energy of the electrons at the depth s is obtained by integrating Eq. (4):

$$E_e(s) = \{[E_e(0)]^{\nu+1} - (\nu+1)\kappa s\}^{\frac{1}{\nu+1}}, \tag{6}$$

where the initial kinetic energy of the electrons $E_e(0) = e \cdot U$, U representing the high voltage of the X-ray tube. The maximum penetration depths h_K and h_{KK} can be deduced from Eq. (6). One finds:

$$h_{K,KK} = \frac{[E_e(0)]^{\nu+1} - [E_{K,KK}]^{\nu+1}}{(\nu+1)\kappa}. \tag{7}$$

The single K-shell ionization threshold energies E_K were taken from the LBNL X-ray data booklet [32], whereas the double K-shell ionization threshold energies E_{KK} were calculated from the following relation:

$$E_{KK}(Z) = 2E_K + \epsilon_K[E_K(Z+1) - E_K(Z)], \tag{8}$$

where ϵ_K is a constant comprised between 0 and 1 which accounts for the increase of the electronic screening resulting from the removal of the first *1s* electron. The value $\epsilon_K = 0.570$ reported in [29] for 3*d* transition elements was adopted. The so-determined maximum penetration depths h_K and h_{KK} are quoted in Table 2.

The energy dependent single K-shell ionization cross sections $\sigma_K(E(s))$ were determined from least squares fits of Gryzinsky-like functions to the experimental values reported by Liu et al. [33]. For Cr, however, the experimental cross sections reported in [33] are given only for electron energies below 25 keV and above 2 MeV so that the fitted Gryzinsky functions for the 60 kV measurements were not reliable. The difficulty was circumvented by calculating the cross sections at 40, 50 and 60 keV by means of the universal function proposed in [34]:

$$\sigma_K E_K^2 u_K = 1.32 \times 10^{-5} b_K [\ln(u_K) + \ln(c_K)], \tag{9}$$

where u_K is a dimensionless parameter defined by $u_K = E_e/E_K$. The

Table 2
Parameters κ and ν describing the electron energy loss, single and double K-shell ionization threshold energies E_K and E_{KK} and maximum penetration depths h_K and h_{KK}.

Anode	U [kV]	κ [MeV$^{(\nu+1)}$/(g/cm^2)]	ν	E_K [keV]	E_{KK} [keV]	h_K [mg/cm^2]	h_{KK} [mg/cm^2]
Sc	20.0	0.551	0.716	4.492	9.254	1.186	0.943
Cr	26.5	0.527	0.714	5.989	12.291	2.024	1.607
Cr	60.0	0.527	0.714	5.989	12.291	8.739	8.323
Cu	39.6	0.507	0.707	8.979	18.346	4.296	3.412

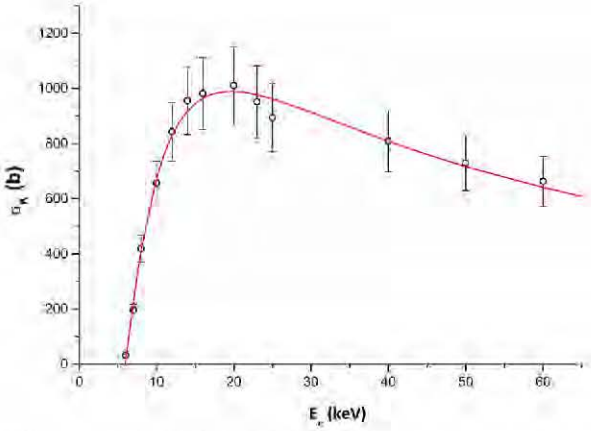

Fig. 6. Variation of the single K-shell ionization cross section as a function of the electron energy for the case of the Cr X-ray tube operated at 60 kV. The data from Refs. [33,34] were fitted with a Gryzinsky-like function (red solid line). For details, see text. (For interpretation of the references to color in this figure legend, the reader is referred to the web version of this article.)

parameters b_K and c_K were adjusted to match Liu's data below 25 keV. For illustration, the variation of σ_K as a function of the electron energy corresponding to the Cr X-ray tube operated at 60 kV is depicted in Fig. 6.

Unfortunately, for the double K-shell ionization cross section the same method could not be applied because, to our best knowledge, no experimental cross sections $\sigma_{KK}(E)$ related to electron impact are available in the literature. The problem was solved by replacing Eq. (2) by the following approximation:

$$\zeta_{K\alpha,K\beta} \cong \frac{\bar{\sigma}_K \int_0^{h_K} e^{-\mu_{K\alpha,K\beta}\mathrm{ctg}(\alpha)s}\mathrm{d}s}{\bar{\sigma}_K h_K}, \tag{10}$$

where $\bar{\sigma}_K$ represents the average value of the cross section σ_K for the anode layer of thickness h_K. Using the above approximation and calculating the integral, one obtains the following simpler expression for the self absorption correction factor:

$$\tilde{\zeta}_{K\alpha,K\beta} = \frac{1 - e^{-\mu_{K\alpha,K\beta}\mathrm{ctg}(\alpha)h_K}}{\mu_{K\alpha,K\beta}\mathrm{ctg}(\alpha)h_K}. \tag{11}$$

For the hypersatellites, a similar expression is obtained:

$$\tilde{\zeta}_{K^h\alpha,K^h\beta} = \frac{1 - e^{-\mu_{K^h\alpha,K^h\beta}\mathrm{ctg}(\alpha)h_{KK}}}{\mu_{K^h\alpha,K^h\beta}\mathrm{ctg}(\alpha)h_{KK}}. \tag{12}$$

The accuracy of the above approximations was probed by comparing for the diagram lines the values obtained for the self absorption correction factors using the exact expression [Eq. (2)] and the simplified one [Eq. (11)]. For Sc, values $\tilde{\zeta}_{K\alpha} = 0.862$ and $\tilde{\zeta}_{K\beta} = 0.889$ were found which are close to the exact values $\zeta_{K\alpha} = 0.877$ and $\zeta_{K\beta} = 0.901$. Similar relative differences of about 1.5% and 3% are found for Cr (26.5 kV measurement) and Cu, respectively, whereas for the 60 kV measurement of Cr the relative deviation is somewhat bigger (5%). In summary, the relative differences between ζ and $\tilde{\zeta}$ are smaller than 5% in all cases and the above approximations are thus quite acceptable

Table 3
Self-absorption correction factors $\tilde{\zeta}$, solid angles Ω, crystal peak reflectivities Π and CCD efficiencies ε_{CCD} for the X-ray lines of interest.

Target	Crystal	Line	$\tilde{\zeta}$	Ω [μsr]	Π	ε_{CCD}
Sc	LiF(200)	$K\alpha_{1,2}$	0.862	5.69	0.829	0.861
		$K^h\alpha_{1,2}$	0.901	6.67	0.584	0.837
		$K\beta_{1,3}$	0.889	5.37	0.680	0.817
		$K^h\beta_{1,3}$	0.539	4.12	0.878	0.784
Cr[a]	Si(220)	$K\alpha_{1,2}$	0.840	3.49	0.799	0.682
		$K^h\alpha_{1,2}$	0.883	3.32	0.834	0.653
Cr[b]	Si(220)	$K\alpha_{1,2}$	0.506	3.49	0.799	0.682
		$K^h\alpha_{1,2}$	0.556	3.32	0.834	0.653
Cr[b]	Ge(220)	$K\alpha_{1,2}$	0.507	8.09	0.819	0.696
		$K^h\alpha_{1,2}$	0.556	7.73	0.851	0.668
Cr[b]	HAPG(004)	$K\alpha_{1,2}$	0.506	43.3	0.206	0.632
		$K^h\alpha_{1,2}$	0.556	43.3	0.217	0.603
Cu	Si(440)[c]	$K\alpha_{1,2}$	0.803	1.14	0.850	0.240
		$K^h\alpha_{1,2}$	0.852	1.03	0.771	0.226

[a] X-ray tube operated at 26.5 kV × 10 mA.
[b] X-ray tube operated at 60 kV × 10 mA.
[c] Si(440) ≡ Si(220) in 2nd order of diffraction.

within the 10% uncertainty assumed for the self absorption corrections. The correction factors $\tilde{\zeta}_{K\alpha,K\beta}$ and $\tilde{\zeta}_{K^h\alpha,K^h\beta}$ are listed in Table 3. For Sc $\tilde{\zeta}_{K^h\beta} < \tilde{\zeta}_{K\beta}$ because the hypersatellite lies above the K-absorption edge, which leads to a significantly bigger absorption coefficient.

3.2.2. Solid angle

In the von Hamos geometry the solid angle of the spectrometer varies with the Bragg angle. As a consequence the hypersatellites and their parent diagram lines correspond to different solid angles and these differences should be accounted for in the determination of the hypersatellite-to-diagram yield ratios. A dedicated X-ray tracing code was developed to calculate the solid angle of the von Hamos spectrometer operated in the standard geometry (see Refs. [35,36]). A modified version of this code was used in the present work. The main modification needed in the code to adapt it to the present setup consisted to replace the distance between the crystal and the sample by the distance between the crystal and the X-ray tube anode. The latter being not vertical like the sample in the standard geometry, the tilt angle α of the anode with respect to the horizontal plane (see Fig. 5) had also to be considered in the calculations.

The solid angles Ω corresponding to the measured diagram and hypersatellite X-ray lines are listed in the fifth column of Table 3. The calculations were performed using weighted average values for the energies of the $K\alpha_{1,2}$ and $K^h\alpha_{1,2}$ doublets. For the $K^h\alpha$ hypersatellite of Sc, the solid angle is bigger than the one of the corresponding diagram line although the distance between the slit and the crystal is larger for the hypersatellite. This is due to the fact that the solid angle is not only proportional to this distance but also to the Darwin width [35] and for Sc the latter is bigger for the hypersatellite than for the diagram line. The Darwin widths were calculated by means of the XOP software package [37] assuming the Si, Ge and LiF crystals to be perfect and the HAPG one mosaic. In the latter case, the Darwin width was replaced in the calculations by the known mosaicity width of the HAPG crystal

(1050 μrad).

3.2.3. Crystal peak reflectivity

As the peak reflectivity Π of the crystal varies as a function of the photon energy, it should also be considered for a correct determination of the hypersatellite-to-diagram line yield ratios. The peak reflectivities of the four crystals were calculated for each transition of interest with the XOP software package [37]. As K X-rays are not polarized, the average values of the peak reflectivities calculated by the XOP code for s-polarized photons (X-rays linearly polarized in the horizontal plane) and p-polarized photons (X-rays linearly polarized in the vertical plane) were used to correct the fitted intensities. The calculated average peak reflectivities Π are reported in the sixth column of Table 3. For p-polarized X-rays, the peak reflectivity tends to zero when the Bragg angle approaches 45°. This explains the rather big difference of the peak reflectivities corresponding to the $K\alpha$ ($\vartheta = 48.8°$) and $K^h\alpha$ ($\vartheta = 44.9°$) lines of Sc observed with the LiF(220) crystal.

3.2.4. CCD efficiency

Above the Si K-edge ($E = 1839$ eV) the CCD efficiency decreases smoothly as a function of the photon energy. For back-illuminated CCD chips, the thickness of the SiO_2 layer which deposits on the front surface of the CCD when the latter is exposed to air is smaller than 1 μm so that the absorption of the X-rays in that thin layer can be neglected. The CCD efficiency ϵ_{CCD} is thus given by the following simple relation:

$$\epsilon_{\mathrm{CCD}} = 1 - \exp\left[-\mu_{\mathrm{Si}}(E)\rho_{\mathrm{Si}}\frac{h_{\mathrm{Si}}}{\sin(\vartheta)}\right], \tag{13}$$

where $\mu_{Si}(E)$ represents the total mass attenuation coefficient of Si for the X-ray energy E, ρ_{Si} the specific weight of Si, h_{Si} the depletion depth of the CCD chip and ϑ the Bragg angle.

The back illuminated CCD camera employed in the present experiment was fully characterized in a previous project [28]. In this former work a depletion depth $h_{Si} = 15$ μm was obtained by fitting with the above formula the experimental efficiencies of the CCD camera for a variety of X-rays ranging from 1 keV to 18 keV.

The CCD efficiencies were calculated with Eq. (13) for the energies of the diagram and hypersatellite lines investigated in the present project, using the mass attenuation coefficients μ_{Si} reported in the XCOM database [21] and the depletion depth h_{Si} obtained in [38]. The results are presented in the seventh column of Table 3.

4. Results and discussion

The measured count rates of the hypersatellite X-ray lines can be written as:

$$I_{K^h\alpha,K^h\beta} = I_e\int_0^{h_{\mathrm{KK}}}\sigma_{\mathrm{KK}}(E_e(s))\mathrm{d}s \times n \times \omega_{K^h\alpha,K^h\beta} \times \tilde{\zeta}_{K^h\alpha,K^h\beta} \times \Omega_{K^h\alpha,K^h\beta} \times \Pi_{K^h\alpha,K^h\beta} \times \epsilon_{K^h\alpha,K^h\beta}, \tag{14}$$

where I_e represents the number of electrons impacting the anode per second, σ_{KK} the double K-shell ionization cross section, h_{KK} the maximum penetration depth of the electrons producing a double K-shell ionization, n the number of anode atoms per unit volume, $\omega_{K^h\alpha,K^h\beta}$ the partial fluorescence yield of the considered hypersatellite line and $\tilde{\zeta}_{K^h\alpha,K^h\beta}$, $\Omega_{K^h\alpha,K\beta}$, $\Pi_{K^h\alpha,K^h\beta}$ and $\epsilon_{K^h\alpha,K^h\beta}$ the corresponding self absorption correction factor, solid angle of the spectrometer, crystal peak reflectivity and CCD efficiency, respectively. The partial fluorescence yield $\omega_{K^h\alpha,K^h\beta}$ is given by:

$$\omega_{K^h\alpha,K^h\beta} = \frac{W_{K^h\alpha,K^h\beta}}{W_{K^h\alpha} + W_{K^h\beta}}\omega_{\mathrm{KK}}, \tag{15}$$

where $W_{K^h\alpha}$ and $W_{K^h\beta}$ stand for the radiative transition probability of the $K^h\alpha$ and $K^h\beta$ hypersatellites and ω_{KK} for the fluorescence yield of the doubly ionized K-shell atom.

Similarly, the measured count rates of the diagram lines read:

$$\begin{aligned} I_{K\alpha,K\beta} &= \frac{I_e}{A}\int_0^{h_K}\sigma_K(E_e(s))\mathrm{d}s \times n \times \omega_{K\alpha,K\beta} \times \tilde{\zeta}_{K\alpha,K\beta} \times \Omega_{K\alpha,K\beta} \times \Pi_{K\alpha,K\beta} \times \epsilon_{K\alpha,K\beta} \\ &= \frac{I_e}{A}\int_0^{h_{\mathrm{KK}}}\sigma_K(E_e(s))\mathrm{d}s \times \frac{\int_0^{h_K}\sigma_K(E_e(s))\mathrm{d}s}{\int_0^{h_{\mathrm{KK}}}\sigma_K(E_e(s))\mathrm{d}s} \times n \times \omega_{K\alpha,K\beta} \times \tilde{\zeta}_{K\alpha,K\beta} \times \Omega_{K\alpha,K\beta} \\ &\quad \times \Pi_{K\alpha,K\beta} \times \epsilon_{K\alpha,K\beta}, \end{aligned} \tag{16}$$

where A represents the attenuation factor of the absorber used for the measurement of the considered diagram line (see Section 2.2).

Note that the contribution of the bremsstrahlung to the production of the observed hypersatellite and diagram X-ray yields was assumed to be negligibly small and thus omitted in Eqs (14) and (16). Actually, this contribution was estimated in [19] and found to be less than 2% of the X-ray yield produced by electron impact, i.e., significantly smaller than the uncertainties related to the X-ray intensities measured in the present work.

Using the definitions

$$\bar{\sigma}_K = \frac{1}{h_{\mathrm{KK}}}\int_0^{h_{\mathrm{KK}}}\sigma_K(E_e(s))\mathrm{d}s \tag{17}$$

$$\bar{\sigma}_{\mathrm{KK}} = \frac{1}{h_{\mathrm{KK}}}\int_0^{h_{\mathrm{KK}}}\sigma_{\mathrm{KK}}(E_e(s))\mathrm{d}s \tag{18}$$

$$\chi = \frac{\int_0^{h_K}\sigma_K(E_e(s))\mathrm{d}s}{\int_0^{h_{\mathrm{KK}}}\sigma_K(E_e(s))\mathrm{d}s} \tag{19}$$

and dividing Eq. (14) by Eq. (16) one finds the relative intensity of the hypersatellite line with respect to its parent diagram line:

$$\frac{I_{K^h\alpha,K^h\beta}}{A \times I_{K\alpha,K\beta}} = \frac{\bar{\sigma}_{\mathrm{KK}}}{\bar{\sigma}_K}\frac{1}{\chi}\frac{\omega_{K^h\alpha,K^h\beta}}{\omega_{K\alpha,K\beta}}\frac{\Omega_{K^h\alpha,K^h\beta}}{\Omega_{K\alpha,K\beta}} \times \frac{\Pi_{K^h\alpha,K^h\beta}}{\Pi_{K\alpha,K\beta}}\frac{\epsilon_{K^h\alpha,K^h\beta}}{\epsilon_{K\alpha,K\beta}}\frac{\tilde{\zeta}_{K^h\alpha,K^h\beta}}{\tilde{\zeta}_{K\alpha,K\beta}}. \tag{20}$$

Finally, the double-to-single K-shell ionization cross section ratio P_{KK}

Table 4
Uncorrected and corrected relative intensities of the measured hypersatellite lines.

Target/crystal	$\frac{I(K^h\alpha_{1,2})}{A\times I(K\alpha_{1,2})}$	$[\frac{I(K^h\alpha_{1,2})}{A\times I(K\alpha_{1,2})}]_{\mathrm{cor}}$	$\frac{I(K^h\beta_{1,3})}{A\times I(K\beta_{1,3})}$	$[\frac{I(K^h\beta_{1,3})}{A\times I(K\beta_{1,3})}]_{\mathrm{cor}}$
Sc/LiF(200)	$1.14(7)\times10^{-4}$	$1.35(20)\times10^{-4}$	$1.08(19)\times10^{-4}$	$1.87(41)\times10^{-4}$
Cr/Si(220)	$0.82(7)\times10^{-4}$	$0.87(14)\times10^{-4}$	–	–
Cr[a]/Si(220)	$1.04(2)\times10^{-4}$	$0.99(13)\times10^{-4}$	–	–
Cr[a]/Ge(220)	$0.84(12)\times10^{-4}$	$0.80(16)\times10^{-4}$	–	–
Cr[a]/HAPG(004)	$0.70(2)\times10^{-4}$	$0.63(8)\times10^{-4}$	–	–
Cu/Si(440)	$0.50(4)\times10^{-4}$	$0.62(10)\times10^{-4}$	–	–

[a] X-ray tube operated at 60 kV × 10 mA.

can be derived from Eq. (20):

$$P_{KK} = \frac{\bar{\sigma}_{KK}}{\bar{\sigma}_K} = \left[\frac{I_{K^h\alpha,K^h\beta}}{A \times I_{K\alpha,K\beta}}\right]_{cor} \frac{\omega_{K\alpha,K\beta}}{\omega_{K^h\alpha,K^h\beta}} \chi, \tag{21}$$

where

$$\left[\frac{I_{K^h\alpha,K^h\beta}}{A\times I_{K\alpha,K\beta}}\right]_{cor} = \frac{I_{K^h\alpha,K^h\beta}}{A\times I_{K\alpha,K\beta}} \frac{\tilde{\zeta}_{K\alpha,K\beta}}{\tilde{\zeta}_{K^h\alpha,K^h\beta}} \frac{\Omega_{K\alpha,K\beta}}{\Omega_{K^h\alpha,K^h\beta}} \times \frac{\Pi_{K\alpha,K\beta}}{\Pi_{K^h\alpha,K^h\beta}} \frac{\epsilon_{K\alpha,K\beta}}{\epsilon_{K^h\alpha,K^h\beta}}. \tag{22}$$

The corrected $K^h\alpha$ and $K^h\beta$ relative intensities which were calculated with the self absorption correction factors, solid angles, crystal peak reflectivities and CCD efficiencies given in Table 3 are presented in Table 4. To show the importance of the corrections, the uncorrected relative intensities are also listed. A relative uncertainty of 5% was assumed for each correction factor except for the self absorption $\tilde{\zeta}$ for which a relative uncertainty of 10% was estimated, due to the additional uncertainty related to the approximation $\tilde{\zeta} \cong \zeta$ made in the calculations (see Section 3.2.1).

For the Cr measurements performed at 60 kV with three different crystals, the corrected intensity ratios should be the same but, as shown by Table 4, there is a large scatter of the results. However, in view of the rather big uncertainties characterizing the three ratios, this scatter is not really surprising. Actually, the standard deviation of the three ratios is 0.15×10^{-4}, a value which is comparable to the average uncertainty of the three measurements which is equal to 0.12×10^{-4}.

The partial fluorescence yields were calculated using the fluorescence yields ω_K for singly ionized atoms from Kostroun [39] and the fluorescence yields ω_{KK} for doubly ionized atoms from Natarajan [40]. The relative transition probabilities $W(K\alpha, K\beta)/[W(K\alpha) + W(K\beta)]$ of the diagram lines were determined from the radiative emission rates quoted by Scofield [41] and the relative transition probabilities $W(K^h\alpha, K^h\beta)/[W(K^h\alpha) + W(K^h\beta)]$ of the hypersatellites from the rates reported for Al and Sc by Costa [26]. The correction factors χ [see Eq. (19)] for the difference in the effective thicknesses of the anode layers contributing to the production of the diagram lines and hypersatellites, respectively, were computed by integrating numerically the Gryzinsky-like functions used to reproduce the variation of σ_K as a function of the electron energy. The values obtained for all these parameters are presented in Table 5.

Finally, inserting above values in Eq. (21), one obtains the double-to-single ionization cross section ratios P_{KK} presented in Table 5. As shown, for Sc the values obtained from the relative intensities of the $K^h\alpha$ and $K^h\beta$ hypersatellites are fully consistent. For the Cr measurements performed at 60 kV, the ratio P_{KK} was calculated from the average relative intensity (0.81×10^{-4}) of the hypersatellites measured with the three crystals using the standard deviation of the three measurements (0.15×10^{-4}) as uncertainty.

In Fig. 7 the P_{KK} values obtained in this work (red circles) are compared with results obtained from other measurements performed with electrons (symbols below the dashed line) and photons (symbols around the solid line). P_{KK} values derived from nuclear electron capture (EC) are also plotted (black squares around the dashed line). In our experiment, the dimensionless parameter $\eta = E_e/E_{KK}$ amounts to about 2.2 (see Table 2) for Sc, Cr (26.5 kV measurement) and Cu, and to about 4.9 for the 60 kV measurement of Cr. As it is more sound to compare the ratios P_{KK} of different elements for the same η, the present Cr value depicted in Fig. 7 corresponds to the 26.5 kV measurement. The P_{KK} ratio deduced from the 60 kV measurement is smaller by about 15% than the value obtained at 26.5 kV. This might indicate than the maximum of P_{KK} occurs below 60 kV but no definitive conclusion can be drawn from this observation since the difference between the two ratios (0.15×10^{-4}) is smaller than the combined uncertainty (0.21×10^{-4}). For Sc, the weighted average [$(1.33 \pm 0.18) \times 10^{-4}$] of the P_{KK} values derived from the relative intensities of the $K^h\alpha$ and $K^h\beta$ hypersatellites is plotted.

Fig. 7 shows that our result for Cr agrees well with the one obtained by Saijonmaa and Rahkonen [19] for a similar excitation energy ($\eta \cong 2$). Furthermore, a power-law fit of the few electron data found in the literature for elements $11 \leq Z \leq 26$ shows an approximate Z^{-2} dependence of P_{KK}. This is well confirmed by our results since a double logarithmic fit of present Sc, Cr and Cu P_{KK} ratios leads to a straight line whose slope is -1.999. Fig. 7 shows further that the P_{KK} values obtained in electron measurements are in average about 7.5 times lower than those obtained with photons. A quantitative explanation of this difference would require the knowledge of the velocity distribution of the primary 1s electrons in the case of electron impact (see below). As the measurement of this distribution was beyond the scope of this work, only qualitative arguments will be discussed hereafter.

For photons the variation with energy of the double-to-single ionization cross section ratio P_{KK} results from the combined influence of the knock-out (KO) and shake-off (SO) processes (see Section 1). It is well established that the KO process dominates near the double K-shell ionization threshold energy and at intermediate photon energies, while shake-off prevails at high photon energies. The knock-out probability P_{KO} grows indeed rapidly from the threshold energy, reaches a maximum value, and decreases then to zero with growing photon energy. The shake-off probability P_{SO} rises also from the threshold but less swiftly than the KO process and tends then towards a maximum value which is called the asymptotic limit of shake-off. The SO limit corresponds to an infinitely fast change of the atomic potential. In photoionization, the rapidity of the potential change is related to the velocity at which the photo-electron leaves the ionized atom so that the SO limit

Table 5
Double-to single ionization cross section ratios P_{KK} obtained in the present work. The fluorescence yields ω_K and ω_{KK} for singly and doubly K-shell ionized atoms, the resulting partial fluorescence yield ratios $\omega_{K^h\alpha,K^h\beta}/\omega_{K\alpha,K\beta}$ and the correction factors χ accounting for the effective source thicknesses are also presented.

Target	ω_K [39]	ω_{KK} [40]	$\frac{W_{K\alpha,K\beta}}{W_{K\alpha}+W_{K\beta}}$ [41]	$\frac{W_{K^h\alpha,K^h\beta}}{W_{K^h\alpha}+W_{K^h\beta}}$ [26]	$\frac{\omega_{K\alpha,K\beta}}{\omega_{K^h\alpha,K^h\beta}}$	χ	P_{KK}
Sc[a]	0.183	0.212[b]	0.900	0.857	0.906	1.118	$1.37(22) \times 10^{-4}$
Sc[c]	0.183	0.212[b]	0.100	0.143	0.604	1.118	$1.26(29) \times 10^{-4}$
Cr	0.276	0.316	0.897	0.852[d]	0.920	1.151	$0.92(16) \times 10^{-4}$
Cr[e]	0.276	0.316	0.897	0.852[d]	0.920	1.035	$0.77(13) \times 10^{-4}$
Cu	0.448	0.478[f]	0.892	0.848[d]	0.986	1.126	$0.69(12) \times 10^{-4}$

[a] $K^h\alpha$ hypersatellite.
[b] Linear interpolation from the values reported for Ca and Ti.
[c] $K^h\beta$ hypersatellite.
[d] Linear extrapolation from the values reported for Al and Sc.
[e] 60 kV measurement.
[f] Linear interpolation from the values reported for Fe and Zn.

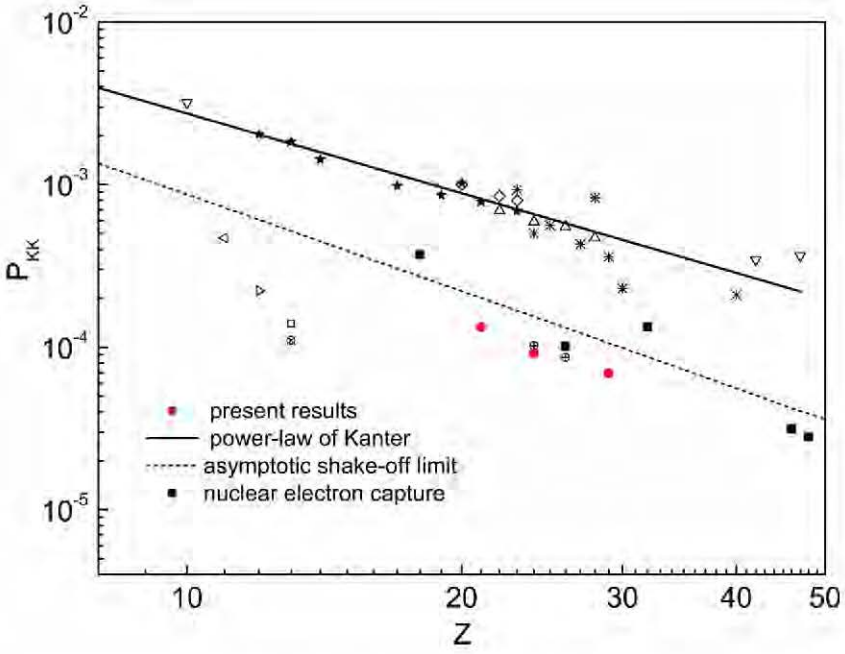

Fig. 7. Double-to-single *K*-shell ionization cross-section ratios versus atomic number for electron impact, photoionization and nuclear electron capture (EC). Electron impact: • present results, ⊕ [19], ▷ [14], ◁ [17], □ [18], ⊗ [4]. Photoionization: ◇ [42], * [43,30], △ [44], ▽ [45], ★ [5]. Nuclear electron capture: ■ [46]. Also shown are the photoabsorption asymptotic limit of Forrey et al. [47] (dashed line) and the power-law fit of Kanter et al. [48,45] of the photoionization data (solid line).

can be determined from the relative intensity of hypersatellites produced by high energy photons. The SO limit can be also determined via the nuclear electron capture decay (EC) in which the first *1s* electron is captured by the nucleus and the second one is ejected as a result of a shake-off process produced by the very fast change of the nuclear Coulomb potential. Such EC nuclear data are plotted in Fig. 7 (black squares) and the least squares fit to these data is represented by the dashed line which is referred to as the photoabsorption asymptotic limit of Forrey [47] in the literature.

Assuming that there is no interference between the KO and SO processes, the ratio P_{KK} can be deduced from the sum of the two probabilities, namely $P_{KK}(E) = P_{KO}(E) + P_{SO}(E)$. As a consequence the P_{KK} increases rapidly with the excitation energy, levels off in the so-called broad maximum region and then drops smoothly with growing energy to reach an asymptotic value corresponding to the limit of Forrey. As shown in Ref. [5], the broad maximum occurs for a scaled excess energy $(E - E_{KK})/Z^{*2} \cong 11$ eV, where Z^* is defined by the simple relation $Z^{*2} \times 13.6\,\text{eV} = E_K$. Using the energies E_K and E_{KK} quoted in Table 2, one finds that for Sc, Cr and Cu this scaled excess energy corresponds to photon energies of 12.9 keV, 17.1 keV and 25.6 keV, respectively. Most of the photon data depicted in Fig. 7 correspond to excitation energies belonging to the broad maximum region. At these energies, the contributions of the knock-out (P_{KO}) and shake-off (P_{SO}) probabilities to the total probability P_{KK} amounts to about 80% and 20%, respectively, and the shake-off probability corresponds to about 80% of its asymptotic limit [5]. As a result, the P_{KK} value at the broad maximum is about 4 times bigger than the shake-off limit. This explains why the photon data presented in Fig. 7 lie significantly above the nuclear EC ones.

In photoionization, the first electron is removed by the photoelectric effect. The kinetic energy of the 1*s* photoelectron is thus equal to $E - E_K$. For photon energies E corresponding to the broad maxima, the kinetic energies of the photoelectrons are thus 8.4 keV, 11.1 keV and 16.6 keV for Sc, Cr and Cu, respectively. In addition, for a given target, all 1*s* photo-electrons have the same energy and therefore all of them contribute to the double ionization. In the case of the *K*-shell ionization induced by electron impact, the atomic electrons are ejected with a continuous energy distribution but most of them leave the atom with small velocities comparable to their orbital velocity even at high excitation energies [49]. In this case, the average kinetic energies of the primary 1*s* electrons are thus about 4.5 keV for Sc, 6.0 keV for Cr and 9.0 keV for Cu, whereas the energies needed to remove the second 1*s* electron are about 4.8 keV for Sc, 6.3 keV for Cr and 9.4 keV for Cu. As a consequence, on the one hand the shake contribution to the double ionization is smaller than for photons and, on the other hand, the KO process is energetically possible only for a fraction of secondary electrons and for those electrons the probability P_{KO} is below its maximum. It is true that, in contrast to photons, electrons can interact sequentially with two bound electrons of the same atom producing a direct double ionization (TS2 process). However, as discussed in Refs. [49,50], the TS2 probability is negligibly small for charged projectiles with a ratio $|Z|/v < 0.05$, where Z stands for the projectile charge and v for the projectile velocity expressed in a.u. In the present experiment, ratios $|Z|/v$ of 0.026 for Sc, 0.023 for Cr and 0.019 for Cu are found, indicating that the contribution of the TS2 process to the electron impact induced double ionization is probably insignificant. For all these reasons one can understand why in Fig. 7 the electron data lie below the photon data and even below the Forrey fit to the nuclear EC data.

In the case of photon impact, the double *K*-shell ionization cross sections can be derived from the following relation:

$$\sigma_{KK}^{\text{photo}} = P_{KK}^{\text{photo}} \sigma_K^{\text{photo}}. \tag{23}$$

The *K*-shell photoabsorption cross sections σ_K^{photo} were derived from a double logarithmic interpolation of the values quoted in the Tables of Scofield [51]. For the energies corresponding to the broad maxima, values of 3230b, 2390b and 1540b were obtained for Sc, Cr and Cu, respectively. The P_{KK}^{photo} ratios were deduced from the power law fit of Kanter $P_{KK}^{\text{photo}}(Z) = 0.12 \times Z^{-1.61}$ [45,48], leading to values of 8.92×10^{-4}, 7.20×10^{-4} and 5.31×10^{-4}. The maximum double *K*-shell ionization cross section induced by photon impact $\sigma_{KK}^{\text{photo}}$ amount thus to 2.88b for Sc, 1.72b for Cr and 0.82b for Cu.

In the case of electron impact, one can write similarly (see Eq. (21)):

$$\bar{\sigma}_{KK} = P_{KK} \bar{\sigma}_K. \tag{24}$$

The average electron-induced single *K*-shell ionization cross section $\bar{\sigma}_K$ is defined in Eq. (17). Using for the $\sigma_K(E_e)$ the cross sections discussed in Section 3.2.1, one finds $\bar{\sigma}_K$ values of 1340b for Sc, 880b for Cr (26.5 kV measurement) and 430b for Cu. From these values and the P_{KK} ratios determined in this work, double *K*-shell ionization cross sections $\bar{\sigma}_{KK}$ of 0.178b, 0.081b and 0.030b are found for Sc, Cr (26.5 kV) and Cu. Note that the latter values are about 15 to 25 times smaller than the corresponding photon double *K*-shell ionization cross sections, whereas the

electron single K-shell ionization cross sections are only about 2.5 to 3.5 times smaller than the single K-shell photoionization cross sections.

5. Summary and concluding remarks

We have investigated the radiative decay of double K-shell vacancy states produced in solid Sc, Cr and Cu thick targets by impact with electrons. The K-hypersatellite X-ray transitions were measured in-house with the von Hamos curved crystal spectrometer of Fribourg operated in the direct geometry, using the Sc, Cr and Cu anodes of the X-ray tubes as targets. The high voltages of the X-ray tubes were chosen so that the kinetic energy E_e of the electrons at the front surface of the anode was about 2 times higher than the threshold energy E_{KK} for the double K-shell ionization. In order to probe the evolution of the relative intensities of the hypersatellites as a function of the electron energy and check the reliability of the experimental setup, the Cr measurements were also performed at a higher voltage (60 kV) and with three different crystals.

The measured hypersatellite spectra were analysed by means of a least-squares fitting program using Voigt profiles to fit the diagram and hypersatellite lines. The major difficulty encountered in the data analysis was related to the poor peak-to-background ratios characterizing the measured hypersatellites and to the bumps observed in the backgrounds of the Sc $K^h\beta$ and Cr $K^h\alpha$ spectra as a result of intensity inhomogeneities of the electron beam spots on the X-ray tube anodes. Despite of this the relative intensities of the hypersatellite transitions could be well determined from the fits.

The P_{KK} ratios were deduced from the relative intensities of the hypersatellites corrected beforehand for the self absorption in the target, energy dependent solid angle of the von Hamos spectrometer, crystal peak reflectivity and CCD efficiency. Our results are well in line with the ratios found in the literature for two $3d$ elements, namely Cr and Fe, that were measured at similar relative electron energies ($\eta = E_e/E_{KK} \cong 2$). A power-law fit of the few electron data found in the literature for elements $11 \leq Z \leq 26$ shows an approximate Z^{-2} dependence of P_{KK} which is well confirmed by our results. The latter were also compared to other experimental ratios obtained with photons and radioactive sources decaying via the nuclear electronic capture (EC). From this comparison, it was found that present P_{KK} ratios deduced from electron impact measurements are about 7.5 times smaller than those obtained by photon impact and that they lie below the EC data, indicating that the electron induced double K-shell ionization probability is even smaller than the high-energy limit of the shake-off probability.

Acknowledgments

The financial support of the Swiss National Science Foundation is acknowledged (Grant No. 200020-146739).

References

[1] P. Richard, W. Hodge, C.F. Moore, Phys. Rev. Lett. 29 (1972) 393.
[2] B. Boschung, J.-Cl. Dousse, B. Galley, C. Herren, J. Hoszowska, J. Kern, C. Rhême, Z. Halabuka, T. Ludziejewski, P. Rymuza, Z. Sujkowski, M. Polasik, Phys. Rev. A 51 (1995) 3650.
[3] M. Kavčič, M. Kobal, M. Budnar, J.-Cl. Dousse, K. Tökési, Nucl. Instrum. Methods Phys. Res. B 233 (2005) 235.
[4] K. Fennane, J.-Cl. Dousse, J. Hoszowska, M. Berset, W. Cao, Y.-P. Maillard, J. Szlachetko, M. Szlachetko, M. Kavčič, Phys. Rev. A 79 (2009) 032708.
[5] J. Hoszowska, J.-Cl. Dousse, W. Cao, K. Fennane, Y. Kayser, M. Szlachetko, J. Szlachetko, M. Kavčič, Phys. Rev. A 82 (2010) 063408.
[6] T. Åberg, J. Utriainen, Phys. Rev. Lett. 22 (1969) 1346.
[7] J.A.R. Samson, W.C. Stolte, Z.-X. He, J.N. Cutler, Y. Lu, R.J. Bartlett, Phys. Rev. A 57 (1998) 1906.
[8] J. Hoszowska, A.K. Kheifets, J.-Cl. Dousse, M. Berset, I. Bray, W. Cao, K. Fennane, Y. Kayser, M. Kavčič, J. Szlachetko, M. Szlachetko, Phys. Rev. Lett. 102 (2009) 073006.
[9] L. Young, E.P. Kanter, B. Krassig, Y. Li, A.M. March, S.T. Pratt, R. Santra, S.H. Southworth, N. Rohringer, L.F. DiMauro, G. Doumy, C.A. Roedig, N. Berrah, L. Fang, M. Hoener, P.H. Bucksbaum, J.P. Cryan, S. Ghimire, J.M. Glownia, D.A. Reis, J.D. Bozek, C. Bostedt, M. Messerschmidt, Nature 466 (2010) 56.
[10] G. Doumy, C. Roedig, S.-K. Son, C.I. Blaga, A.D. DiChiara, R. Santra, N. Berrah, C. Bostedt, J.D. Bozek, P.H. Bucksbaum, J.P. Cryan, L. Fang, S. Ghimire, J.M. Glownia, M. Hoener, E.P. Kanter, B. Krässig, M. Kuebel, M. Messerschmidt, G.G. Paulus, D.A. Reis, N. Rohringer, L. Young, P. Agostini, L.F. DiMauro, Phys. Rev. Lett. 106 (2011) 083002.
[11] B. Rudek, S.-K. Son, L. Foucar, S.W. Epp, B. Erk, R. Hartmann, M. Adolph, R. Andritschke, A. Aquila, N. Berrah, C. Bostedt, J. Bozek, N. Coppola, F. Filsinger, H. Gorke, T. Gorkhover, H. Graafsma, L. Gumprecht, A. Hartmann, G. Hauser, S. Herrmann, H. Hirse-mann, P. Holl, A. Homke, L. Journel, C. Kaiser, N. Kimmel, F. Krasniqi, K.-U. Kuhne, M. Matysek, M. Messerschmidt, D. Miesner, T. Moller, R. Moshammer, K. Nagaya, B. Nilsson, G. Potdevin, D. Pietschner, C. Reich, D. Rupp, G. Schaller, I. Schlichting, C. Schmidt, F. Schopper, S. Schorb, C.-D. Schroter, J. Schulz, M. Simon, H. Soltau, L. Struder, K. Ueda, G. Weidenspointner, R. Santra, J. Ullrich, A. Rudenko, D. Rolles, Nat. Photon 6 (2012) 858.
[12] K. Tamasaku, M. Nagasono, H. Iwayama, E. Shigemasa, Y. Inubushi, T. Tanaka, K. Tono, T. Togashi, T. Sato, T. Katayama, T. Kameshima, T. Hatsui, M. Yabashi, T. Ishikawa, Phys. Rev. Lett. 111 (2013) 043001.
[13] H. Yoneda, Y. Inubushi, M. Yabashi, T. Katayama, T. Ishikawa, H. Ohashi, H. Yumoto, K. Yamauchi, H. Mimura, H. Kitamura, Nat. Commun. 5 (2014) 5080.
[14] E. Mikkola, O. Keski-Rahkonen, R. Kuoppala, Phys. Scr. 19 (1979) 29.
[15] S.I. Salem, Phys. Rev. A 21 (1980) 858.
[16] J.P. Briand, A. Touati, M. Frilley, P. Chevallier, A. Johnson, J.P. Rozet, M. Tavernier, S. Shafroth, M.O. Krause, J. Phys. B: At. Mol. Phys. 9 (1976) 1055.
[17] J. Lahtinen, O. Keski-Rahkonen, Phys. Scr. 27 (1983) 334.
[18] O. Keski-Rahkonen, E. Mikkola, K. Reinikainen, M. Lehkonen, J. Phys. C: Solid State Phys. 18 (1985) 2961.
[19] J. Saijonmaa, O. Keski-Rahkonen, Phys. Scr. 17 (1978) 451.
[20] J. Hoszowska, J.-Cl. Dousse, J. Kern, C. Rhême, Nucl. Instrum. Methods Phys. Res. A 376 (1996) 129.
[21] http://www.nist.gov/pml/data/xcom/.
[22] G.K. Wertheim, M.A. Butler, K.W. West, D.N.E. Buchanan, Rev. Sci. Instrum. 45 (1974) 1369.
[23] A.M. Costa, M.C. Martins, J.P. Santos, P. Indelicato, F. Parente, J. Phys. B: At. Mol. Phys. 40 (2007) 57.
[24] F. Bloch, Phys. Rev. 48 (1935) 187.
[25] C. Herren, J.-Cl. Dousse, Phys. Rev. A 53 (1996) 717.
[26] A.M. Costa, M.C. Martins, J.P. Santos, P. Indelicato, F. Parente, J. Phys. B: At. Mol. Phys. 39 (2006) 2355.
[27] F. Larkins, At. Data Nucl. Data Tables 20 (1977) 311.
[28] J. Campbell, T. Papp, At. Data Nucl. Data Tables 77 (2001) 1.
[29] R. Diamant, S. Huotari, K. Hämäläinen, R. Sharon, C.C. Kao, M. Deutsch, Phys. Rev. A 79 (2009) 062511.
[30] S. Huotari, K. Hämäläinen, R. Diamant, R. Sharon, C.-C. Kao, M. Deutsch, J. Electron Spectrosc. Relat. Phenom. 137-140 (2004) 293 iCESS-9 Proceedings of the 9th International Conference on Electronic Spectroscopy and Structure.
[31] https://physics.nist.gov/PhysRefData/Star/Text/ESTAR.html, 2017.
[32] G.P. Williams, Electron Binding Energies, X-Ray Data Booklet, Lawrence Berkeley National Laboratory, 2009, p. 1.
[33] M. Liu, Z. An, C. Tang, Z. Luo, X. Peng, X. Long, At. Data Nucl. Data Tables 76 (2000) 213.
[34] J.H. Paterson, J.N. Chapman, W.A.P. Nicholson, J.M. Titchmarsh, J. Microsc. 154 (1989) 1, https://doi.org/10.1111/j.1365-2818.1989.tb00563.x.
[35] Yves-Patrik Maillard, PhD thesis No 1995, Physics Department, December, University of Fribourg, Switzerland, 2016.
[36] Y.-P. Maillard, J.-Cl. Dousse, J. Hoszowska, M. Berset, O. Mauron, P.-A. Raboud, M. Kavčič, J. Rzadkiewicz, D. Banaś, K. Tökési, Phys. Rev. A 98 (2018) 012705.
[37] M. Sanchez del Rio, R.J. Dejus, http://www.esrf.eu/UsersAndScience/Experiments/TBS/SciSoft/xop2.3/ (2011).
[38] J. Szlachetko, J.-Cl. Dousse, J. Hoszowska, M. Berset, W. Cao, M. Szlachetko, M. Kavčič,, Rev. Sci. Instrum. 78 (2007) 093102, https://doi.org/10.1063/1.2779214.
[39] V.O. Kostroun, M.H. Chen, B. Crasemann, Phys. Rev. A 3 (1971) 533.
[40] L. Natarajan, Phys. Rev. A 78 (2008) 052505.
[41] J.H. Scofield, At. Data Nucl. Data Tables 14 (1974) 121.
[42] M. Oura, H. Yamaoka, K. Kawatsura, K. Takahiro, N. Takeshima, Y. Zou, R. Hutton, S. Ito, Y. Awaya, M. Terasawa, T. Sekioka, T. Mukoyama, J. Phys. B: At. Mol. Opt. Phys. 35 (2002) 3847.
[43] S. Huotari, K. Hämäläinen, R. Diamant, R. Sharon, C.C. Kao, M. Deutsch, Phys. Rev. Lett. 101 (2008) 043001.
[44] J. Ahopelto, E. Rantavuori, O. Keski-Rahkonen, Phys. Scr. 20 (1979) 71.
[45] E.P. Kanter, I. Ahmad, R.W. Dunford, D.S. Gemmell, B. Krässig, S.H. Southworth, L. Young, Phys. Rev. A 73 (2006) 022708.
[46] A. Suzuki, J. Law, Phys. Rev. C 25 (1982) 2722.
[47] R.C. Forrey, H.R. Sadeghpour, J.D. Baker, J.D. Morgan, A. Dalgarno, Phys. Rev. A 51 (1995) 2112.
[48] E.P. Kanter, R.W. Dunford, B. Krässig, S.H. Southworth, Phys. Rev. Lett. 83 (1999) 508.
[49] J.H. McGuire, N. Berrah, R.J. Bartlett, J.A.R. Samson, J.A. Tanis, C.L. Cocke, A.S. Schlachter, J. Phys. B: At. Mol. Opt. Phys. 28 (1995) 913.
[50] A.S. Schlachter, J.A. Tanis, Phys. Rev. Lett. 73 (1994) 3596.
[51] J.H. Scofield, Lawrence Livermore Laboratory Report UCRL-51326, Livermore CA, 1973.